

Unravelling calcite-to-aragonite evolution from a subsurface fluid - Formation pathway, interfacial reactions and nucleation effects

Stefanie Eichinger^{a,**}, Ronny Boch^{a,b,*}, Andre Baldermann^a, Katja Goetschl^a, Robert Wenighofer^c, René Hoffmann^d, Franziska Stamm^a, Dorothee Hippler^a, Cyrill Grengg^a, Adrian Immenhauser^{d,e}, Martin Dietzel^a

^a Institute of Applied Geosciences, Graz University of Technology & NAWI Graz GeoCenter, Rechbauerstraße 12, 8010 Graz, Austria

^b Geoconsult ZT GmbH, Wissenspark Salzburg Urstein, Urstein Süd 13, 5412 Puch bei Hallein, Austria

^c Montanuniversität Leoben, Department Zentrum am Berg, Franz Josef Straße 18, 8700 Leoben, Austria

^d Institute for Geology, Mineralogy and Geophysics, Ruhr-Universität Bochum, Universitätsstraße 150, D-44801 Bochum, Germany

^e Fraunhofer Research Institution for Energy Infrastructures and Geothermal Systems IEG, Am Hochschulcampus 1, 44801 Bochum, Germany

ARTICLE INFO

Editor: Karen Johannesson

Keywords:

Calcite-aragonite transition
Environmental monitoring
Mg/calc ratio
Carbon dioxide degassing
CaCO₃ polymorphism

ABSTRACT

Calcite-aragonite alternations are documented in sedimentary deposits worldwide, but their formation is still poorly understood and individual CaCO₃ precipitation pathways are rarely confirmed experimentally. Therefore, (sub)recent CaCO₃ sinter formation in a historic subsurface adit at Erzberg (Austria) was used as a natural laboratory to monitor and assess the calcite-to-aragonite evolution pathway and intergrowth mechanism in terms of solid-liquid-atmosphere dynamics and their relevance for solid-liquid interface reactions and nucleation effects. Our results indicate an initial homogeneous nucleation of low-Mg calcite (LMC: $\sim 3 \pm 1$ mol% MgCO₃), induced by CO₂ degassing from the percolating geogenic fluid, which is originated from seepage of local meteoric water and incongruent dissolution of Mg-Ca-Fe-bearing minerals from the host rock. Progressive LMC growth leads to an increase in the aqueous molar ratio of Mg/Ca, causing a Mg/Ca zonation pattern with transitions to high-Mg calcite (HMC: up to 7 mol% MgCO₃). At a critical Mg concentration, the available Mg calcite crystal surfaces are acting as a nucleation site for heterogeneous aragonite formation. In this way, fast growing acicular aragonite crystals are initiated, which impede further calcite growth. The calcite-to-aragonite transition is thus controlled by the reaction kinetics and mechanisms of Mg-calcite formation and the chemical evolution of the precipitating solution at the nano- to micro-spatial scale, creating Mg-enriched HMC surface sites for aragonite to be nucleated and preferentially grown. In the present case, the dynamics of the formation of calcite-aragonite sequences are triggered by distinct local environmental changes, in particular seasonal variations in seepage fluid flow behavior and progress in CO₂ degassing. These considerations are relevant for a better understanding of proxy signal development and preservation in calcareous sedimentary sequences forming under highly dynamic environmental conditions.

1. Introduction

Aragonite is the high-temperature modification of anhydrous calcium carbonate minerals (e.g. Jamieson, 1953; Plummer and Busenberg (1982), but well known to be precipitating as an unstable phase in aqueous media at near Earth's surface conditions, particularly in marine and terrestrial settings (e.g. Frisia et al., 2002; Stanley, 2006; Dove et al., 2003; Falini et al., 2013; Wassenburg et al., 2016). The nucleation and

growth of aragonite versus calcite in the latter surroundings have been attributed to various factors, like pH, fluid Mg/Ca ratio, pCO₂, the degree of supersaturation and diverse strategies to inhibit calcite nucleation and growth (e.g. Fyfe et al., 1965; Perdikouri et al., 2011; Swart, 2015; Wassenburg et al., 2012; Boon et al., 2020), where reaction mechanisms and environmental controls are still not fully understood. In particular, Mg²⁺ ions are well-known to promote aragonite over calcite nucleation and crystal growth in comparable low temperature settings

* Corresponding author at: Institute of Applied Geosciences, Graz University of Technology & NAWI Graz GeoCenter, Rechbauerstraße 12, 8010 Graz, Austria.

** Corresponding author.

E-mail addresses: Stefanie.eichinger@tugraz.at (S. Eichinger), ronny.boch@tugraz.at (R. Boch).

<https://doi.org/10.1016/j.chemgeo.2023.121768>

Received 8 July 2023; Received in revised form 2 October 2023; Accepted 4 October 2023

Available online 9 October 2023

0009-2541/© 2023 The Authors. Published by Elsevier B.V. This is an open access article under the CC BY license (<http://creativecommons.org/licenses/by/4.0/>).

(e.g. Riechelmann et al., 2014; Rossi and Lozano, 2016; Purgstaller et al., 2017; Boch et al., 2019). Although calcite versus aragonite formation is documented and evaluated in a large number of studies, the monitoring and assessment of the individual CaCO_3 formation mechanisms in field-based laboratories are still rare (e.g. Riechelmann et al., 2014; Rossi and Lozano, 2016; Drake et al., 2018).

We investigated active CaCO_3 sinter precipitation in a historic sub-surface adit of the Ca-Mg-Fe carbonate iron ore hosted at Erzberg as a natural laboratory to study calcite-to-aragonite evolution and inter-growth. The Erzberg iron ore mine hosts the largest siderite deposit in the world and further comprises prominent secondary calcite-aragonite as well as dolomite precipitates (Prochaska, 2012; Baldermann et al., 2020). The latter Ca-Mg-bearing carbonate minerals are precipitating at low temperatures (0 to 10 °C) from meteorically-derived geogenic Mg^{2+} ion-rich fluids (Boch et al., 2019).

In the present study, for the first time, the formation of differentiated, actively precipitating calcite-aragonite mineral sequences is documented in-situ. The CaCO_3 precipitates and related aqueous solutions were collected from a flow through sinter basin located in a side corridor of the historic adit. The samples were analyzed using a broad range of bulk and high-resolution optical, mineralogical and chemical tools, such as X-ray diffraction (XRD), cathodoluminescence (CL), Raman spectroscopy, scanning electron microscopy (SEM) and electron probe microanalysis (EPMA). An automated sensor system was also implemented in the sinter basin for the in-situ monitoring of active CaCO_3 precipitation including continuous, time-resolved measurements

of the aqueous fluid and air temperature, relative humidity and atmospheric CO_2 concentration. Additionally, sample holders with preloaded calcite and aragonite seeds were exposed to the seepage fluid in the sinter basin in order to stimulate and assess active CaCO_3 precipitation via field laboratory monitoring and analysis. The aim of this study is to develop a conceptual model that explains the recurrent and competitive formation of calcite versus aragonite sinter.

2. Study site and monitoring strategy

The Erzberg iron ore deposit is part of the Northern Grauwackenzone, documenting the sedimentary cover of the Upper Central Austroalpine Basement (e.g. Froitzheim et al., 2008; Fig. 1A). The Northern Grauwackenzone underlies the Northern Calcareous Alps and consists of various differentiated nappe systems (Schönlaub, 1982; Schmid et al., 2004). The Northern Grauwackenzone in the study area consists of Silurian to Devonian limestones and Carboniferous schists, which host the dominant siderite and ankerite ($\text{Ca}(\text{Fe},\text{Mg},\text{Mn})(\text{CO}_3)_2$) ore body (e.g. Thalmann, 1979; Schönlaub, 1982; Schulz et al., 1997; Prochaska, 2012).

In the upper south-western part of the Erzberg iron ore deposit a new interdisciplinary tunnel research centre, referred to as “Zentrum am Berg”, is situated (ZaB; Fig. 1A). In its vicinity numerous historic sub-surface mining adits, which remained undiscovered for a long time, were found. One of the major historic adits is the “Presserstollen”, in which CaCO_3 precipitates formed more or less undisturbed over an

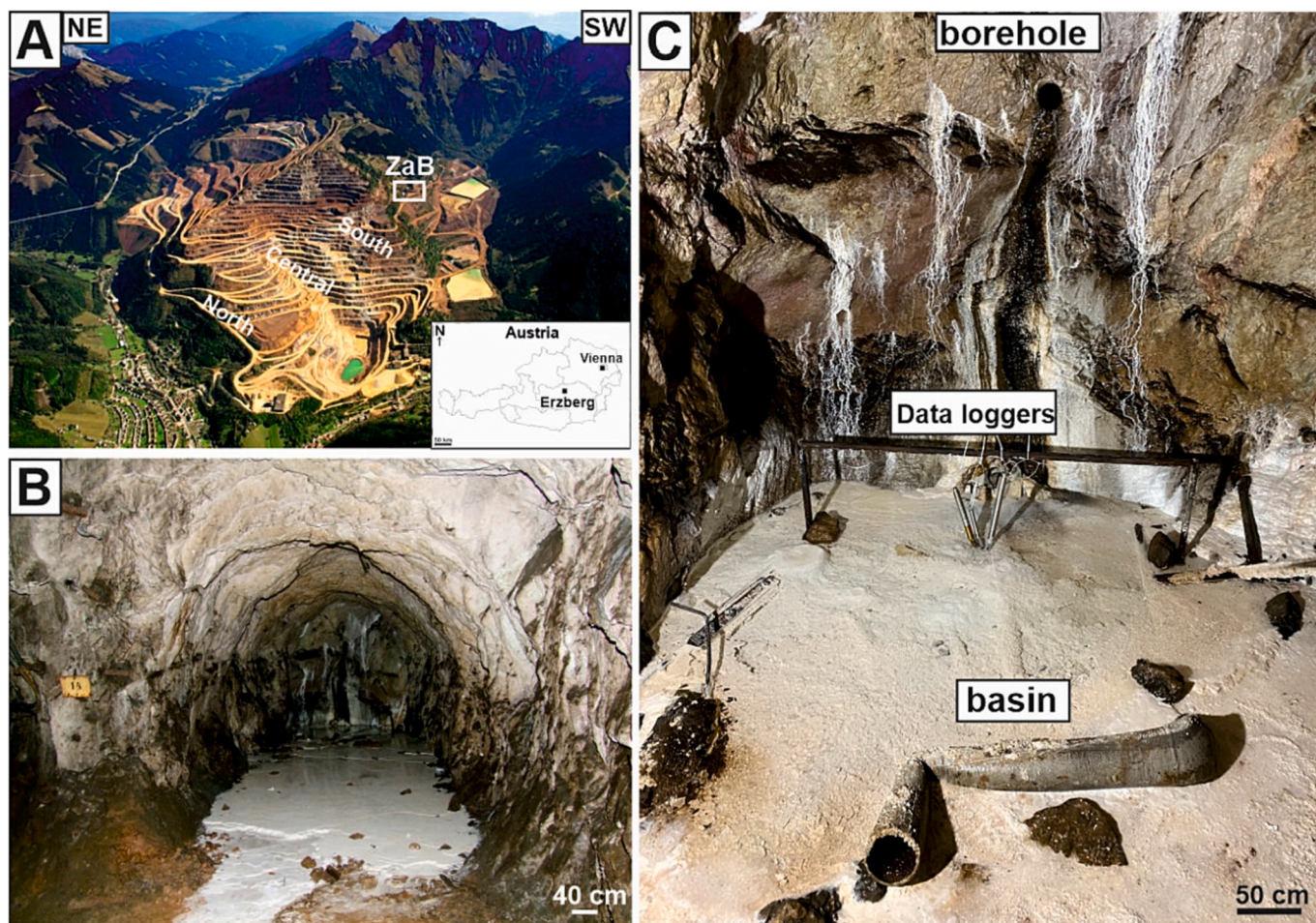


Fig. 1. (A) Overview of the Erzberg iron ore mine (Austria). The tunnel research center “Zentrum am Berg” (ZaB) is located on the upper south-western part of the Erzberg. (B) This research facility hosts a historic mining site, the “Presserstollen”, in which undisturbed CaCO_3 precipitates form in a sinter basin fed by seepage water. (C) Close-up of the examined sinter basin, the adjacent host rock and the incoming water supply via a borehole. The rack in the back part of the sinter basin shows the water monitoring system with the data loggers (e.g. fluid temperature).

extended time interval. Historic documents report an age of the “Presserstollen” of ~150 years (Fig. 1B). It has a length of ~1500 m and is located at approximately 1100 m above sea level. The investigated solid and aqueous samples were recovered from an active sinter basin (200 × 200 × 7 cm width, length and depth) from a side corridor of this historic main adit. The inflowing aqueous solution was sampled repeatedly and is referred to as “borehole” sample, whereas the solution sampled from the sinter basin itself is called the “basin” sample (Fig. 1C). The major solid sample considered here is termed “Erz” (named after the Erzberg study site) and was taken from the central area of this sinter basin during the first sampling campaign. The analyzed precipitates and associated aqueous solutions from the borehole and sinter basin, respectively, were collected during 10 individual sampling campaigns between May 2021 and September 2022. The sensors for the fluid temperature and air measurements (atmospheric CO₂, relative humidity and air temperature) were installed later in February 2022. During each sampling visit, the pH, fluid temperature and specific conductivity were measured in the aqueous solution of the borehole and the sinter basin as well as the volume of the fluid inflow at the borehole.

For the in-situ CaCO₃ precipitation experiments, specifically-designed sample holders (Arbeiter et al., 2019) were pretreated and preloaded with either aragonite or calcite seed crystals (aragonite: synthesized as described in Mavromatis et al. (2018); calcite: purchased from Carl Roth), to study the relevance of potential substrate/seed effects on CaCO₃ polymorphism. All seeds were pre-flushed with ethanol and subsequently exposed to the sinter basin during a sampling campaign in April 2022. After one week of exposure in the sinter basin, the sample holders were recovered, dried at 40 °C and examined using SEM analysis (see below). The fluid chemistry and the inflowing volume were measured shortly before and after exposure of the sample holders.

3. Analytical methods

3.1. Characterization of solids

The actively precipitating CaCO₃ varieties from the sinter basin were photographed using a digital camera (Fig. 2A & B) and reflected-light microscopy (Fig. 2C & D) in order to document their macro- and microscopic appearance. Sub-samples were taken using the micro-drilling technique across the vertical profile of sample “Erz”. Aliquots

of the precipitates were dried at 40 °C and subsequently ground in preparation for XRD analyses using a PANalytical X’Pert Pro diffractometer equipped with a Co-K α -radiation source (40 mA, 40 kV) applied at a 2 θ range from 4 to 85°. The mineralogical composition (uncertainty: ± 3 wt%) of the samples was evaluated quantitatively by Rietveld refinement using the PANalytical X’Pert HighScore Plus software (version 3.0.4 with the PDF-4 database).

Additionally, small pieces of the precipitates were mounted on standard samples holders, gold/palladium-coated and subsequently imaged using a Zeiss DSM 982 Gemini SEM operated at 2 kV accelerating voltage for detailed petrographic studies. Qualitative high-resolution elemental distribution maps of Mg, together with backscattered electron imaging (BSE) of the same areas, were recorded by EPMA using a JEOL JXA8530F Plus Hyper Probe, equipped with a field emission gun. The wavelength-dispersive analytical mode with 15 kV acceleration voltage, a beam current of 10 nA and a pixel size of 3 × 3 μ m were chosen for these measurements.

The sample “Erz” was also analyzed using a HCl-LM CL microscope equipped with a hot cathode operated at 14 kV acceleration voltage and 0.1 mA probe current (Hoffmann et al., 2016). For this analysis, a thin section (~10 μ m thick) of the sample was coated with a super-thin (~10 nm) gold layer and analyzed by linearly polarised light (lpl) as well as by CL imaging.

Raman spectra of calcite at the transition to aragonite domains were collected using a WITec® alpha300R Raman spectrometer at the Institute for Earth Sciences (University of Graz). The instrument is equipped with a WITec® alpha300 microscope, a thermoelectrically cooled (–55 °C) CCD camera and an automated x-y-z stage. A diode pumped solid-state laser at 532 nm (30 mW) with 2400 grooves/mm grating and a × 100/0.9 Zeiss objective with a working distance of 1 mm and a laser spot size of <2 μ m were used to acquire Raman spectra in a range from 100 to 800 cm^{–1}. Four line scans of up to 55 μ m length were recorded in 2–5 μ m intervals with a laser power of 20 mW at an integration time of 0.5 s and 20 accumulations. An Ar/Hg lamp was also used to record a steady Raman band at ~479.4 cm^{–1} (± 0.1 cm^{–1}; 2SD). Cosmic rays and background for all spectra were removed using the WITec Control SIX Software. A peak fit was performed to determine the exact peak positions by applying a PseudoVoigt function to the ~281 cm^{–1} and ~479.4 cm^{–1} Raman bands using the *fityk* software, with an accuracy of ~0.2 cm^{–1}. Subsequently, the MgCO₃ content of calcite was determined

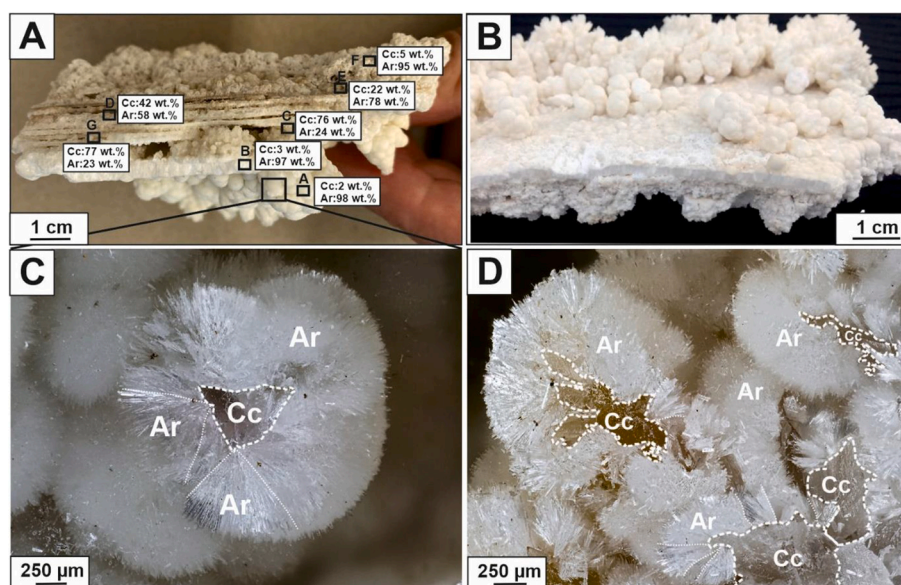


Fig. 2. Macroscopic appearance and detailed mineralogical composition of a representative CaCO₃ precipitate (“Erz”) collected from the active sinter basin at Erzberg. (A) The sample is laminated, with alternating porous and dense layers made of aragonite and calcite. (B) Close-up of the bottom side of the sample shows cauliflower-like to bulbous CaCO₃ structures, which have an inner core made of calcite (Cc) that is surrounded by bundles of acicular aragonite (Ar) crystals (C & D).

by applying the linear relationship between the peak shift of the ν_3 band and the Mg content of calcite, with an estimated analytical uncertainty of <1 mol% MgCO_3 (Borromeo et al., 2017).

3.2. Aqueous solutions

On-site measurements of the fluids from the borehole and the sinter basin included pH, specific conductivity (SpC: $\mu\text{S}/\text{cm}$), fluid temperature ($^{\circ}\text{C}$) as well as the discharge from the borehole. These measurements were conducted using a handheld WTW pH/Con 3320 instrument connected to a TetraCon 325 probe and a WTW SenTix 41 pH probe. Standard buffer solutions of pH 4, 7 and 10 (Merck) were applied for pH calibration, yielding an uncertainty of ± 0.05 pH units (Eichinger et al., 2020). Additionally, data loggers from Driesen and Kern (DK- μS -Log3040 and DK660) were implemented for the in-situ monitoring, including continuous measurements of the aqueous fluid and air temperature, relative humidity and atmospheric CO_2 , enabling on-site tracking of these parameters (Boch et al., 2022). The data logger or probe were placed into the sinter basin and recorded the fluid temperature continuously, i.e., in intervals of 5 min between February and July 2022. The probes recording the air temperature ($^{\circ}\text{C}$), relative humidity (%) and atmospheric CO_2 (in ppm) were installed on the adjacent tunnel wall above the sinter basin and were operated continuously in intervals of 15 min from February 2022 to July 2022.

After sampling, the aqueous solutions were filtered (0.45 μm cellulose acetate filters) immediately and filled in gas-tight borosilicate glass bottles. Major cations (Na^+ , K^+ , Mg^{2+} and Ca^{2+}) and anions (Cl^- and SO_4^{2-}) were analyzed by ion chromatography (Thermo Fisher Dionex ICS-3000) with an analytical uncertainty of $\pm 3\%$. Pore fluids from the sample “Erz” were expressed by micropipettes and subsequently the Ca and Mg concentrations measured in μL -vials by ion chromatography. The samples for titration (alkalinity given as HCO_3^-) were measured in the laboratory within 4 h after sampling (Schott TitroLine alpha plus titrator) using a 0.02 M HCl stock solution with an analytical uncertainty of $\pm 2\%$. Filtrated samples for minor and trace elements, including Si, Al, Ba, Sr and Fe, were filled in 50 mL PE vials that were preloaded with 1 mL suprapure HNO_3 solution (69%). The solutes were measured with a PerkinElmer Optima 8300 DV ICP-OES calibrated against the NIST 1643f reference material and in-house standards at an analytical uncertainty of $\pm 5\%$.

Fluid samples for light stable isotope measurements ($\delta^2\text{H}_{\text{H}_2\text{O}}$ and $\delta^{18}\text{O}_{\text{H}_2\text{O}}$) were taken only once and analyzed by wavelength-scanned cavity ring-down spectroscopy (WS-CRDS) using a L2120-I system (Picarro) at the isotope laboratory of JR-AquaConSol GmbH in Graz. Results of the isotopic measurements are given in per mil (‰) with respect to Vienna Standard Mean Ocean Water (VSMOW), using the standard delta notation. The analytical uncertainties are $\pm 0.8\text{‰}$ and $\pm 0.08\text{‰}$ for $\delta^2\text{H}$ and $\delta^{18}\text{O}$, respectively (cf. Boch et al., 2019).

Hydrochemical modelling was performed using the computer code PHREEQC (version 3.1.7.9213; Parkhurst and Appelo, 2013) based on in-situ measured and laboratory analyzed water parameters. The database phreeqc.dat was used for calculating ion activities and elemental speciation, selected saturation indices (SI means $\text{SI} = \log [\text{IAP}/\text{Ksp}]$; IAP: ion activity product, Ksp: solubility product) for calcite ($\text{SI}_{\text{calcite}}$), vaterite ($\text{SI}_{\text{vaterite}}$; solubility constant from Plummer and Busenberg, 1982), aragonite ($\text{SI}_{\text{aragonite}}$), dolomite ($\text{SI}_{\text{dolomite}}$), amorphous CaCO_3 (SI_{ACC} ; solubility constant from Brecevic and Nielsen, 1989) and ikaite ($\text{SI}_{\text{ikaite}}$; solubility constant from Bischoff et al., 1993), ion charge balances and the internal partial pressure of CO_2 ($p\text{CO}_2$ in atm.).

4. Results and interpretation

4.1. Mineral precipitates

4.1.1. Morphology and mineralogy

Sample “Erz” shows a spatially differentiated macroscopic

appearance (crystal growth, porosity; cf. Fig. 2). It consists of several plate-like and compact horizontal layers that are repeatedly interrupted by subtle layers of small, spherical crystal structures (Fig. 2A). The bottom side of the sample also shows well-developed spherical structures that vary significantly in size (Fig. 2B), while the top part of the sample shows finer roundish structures. The spherical crystal shapes on the bottom side consist of calcitic cores with aragonite growing on their outer surface. Calcite typically shows elongated or rhombohedral crystals shapes, whereas the aragonite crystals are mostly acicular in appearance (Fig. 2C & 2D). The top side of the sample is visually characterized by white to beige colors, while the bottom side is snow-white in colour (Fig. 2A).

Detailed (spot wise) mineralogical analyses using XRD, CL and Raman confirm the highly differentiated appearance of the sample and reveal a predominant and recurrent combination of the two CaCO_3 polymorphs calcite and aragonite (Fig. 2A, sub-samples A - G). The aragonite and calcite proportions vary strongly across the sample, such as between distinct layers and individual crystal aggregates: the aragonite content varies between 23 and 98 wt%, whereas the calcite content ranges from 2 to 77 wt. The calcite is a low-Mg calcite (LMC: <4 mol% MgCO_3), with MgCO_3 contents varying between 1.5 and 3.5 mol% based on the peak position of the calcite 104-reflection as well as the evaluation of Raman spectra (Lumsden and Chimahusky, 1980; Borromeo et al., 2017).

4.1.2. Petrographic and microstructural characterization

Petrographic and microstructural characterization of the sample “Erz” via SEM and CL analyses confirm the intimate coexistence of the two CaCO_3 polymorphs aragonite and calcite (Fig. 3). The SEM images show that aragonite typically precipitates in acicular shapes preferentially on preexisting surfaces of the calcite crystals (Fig. 3A & 3B). Calcite crystals typically reveal a rough, mottled surface and idiomorphic (mostly rhombohedral) crystal morphologies (Fig. 3A & 3B). The CL images support the observation that aragonite (luminescence features are always bluish) grows from a predetermined calcite substrate (luminescence features are orange to red). Calcite crystals often show an elongated morphology as well as some internal zonation, which is partly interrupted by the nucleation and intergrowth of acicular shaped aragonite crystals (Fig. 3C - 3F). The widespread elongated calcite crystals are relatively large (400 μm up to 1.5 mm), whereas the distinctly rhombohedral calcite crystals are typically smaller (~ 200 μm). Aragonite crystals vary strongly in their size with lengths of up to ~ 600 μm .

4.1.3. Geochemical composition

BSE imaging, quantitative chemical data and elemental distribution maps of Mg from different parts of the sample “Erz” document that the highly variable Mg concentration is closely related to the spatial occurrence and distribution of calcite and aragonite (Fig. 4). Calcite crystals are clearly indicated by elevated Mg contents, while aragonite crystals typically contain very low Mg (see also Böttcher and Dietzel, 2010). The calcite crystals appear with some internal zonation of increasing Mg concentration in growth direction and the aragonite crystals nucleate from elevated Mg levels preferentially (Fig. 4B & 4D). Moreover, detailed spatially-resolved chemical analysis of a single calcite crystal reveals the transformation from a dense LMC (<4 mol% MgCO_3) to a HMC before the aragonite crystals nucleate initially and then continue to grow with different crystal shape (acicular and spherical) and higher porosity (Fig. 4C). The MgCO_3 contents vary between 3.1 and 3.9 mol% within the core regions of calcite and increase to up to 4.8 mol% MgCO_3 at the calcite-aragonite transitional contact/zone, which is referred to as a HMC (>4 mol% MgCO_3). In analogy, micro-Raman line scans show (Fig. 4F) a shift from LMC to HMC within a similar range of the MgCO_3 contents up to 4.8 mol% MgCO_3 by entering the outer calcite crystal area closer to the calcite/aragonite interface. Thus, both spatially-resolved chemical and spectroscopic analyses

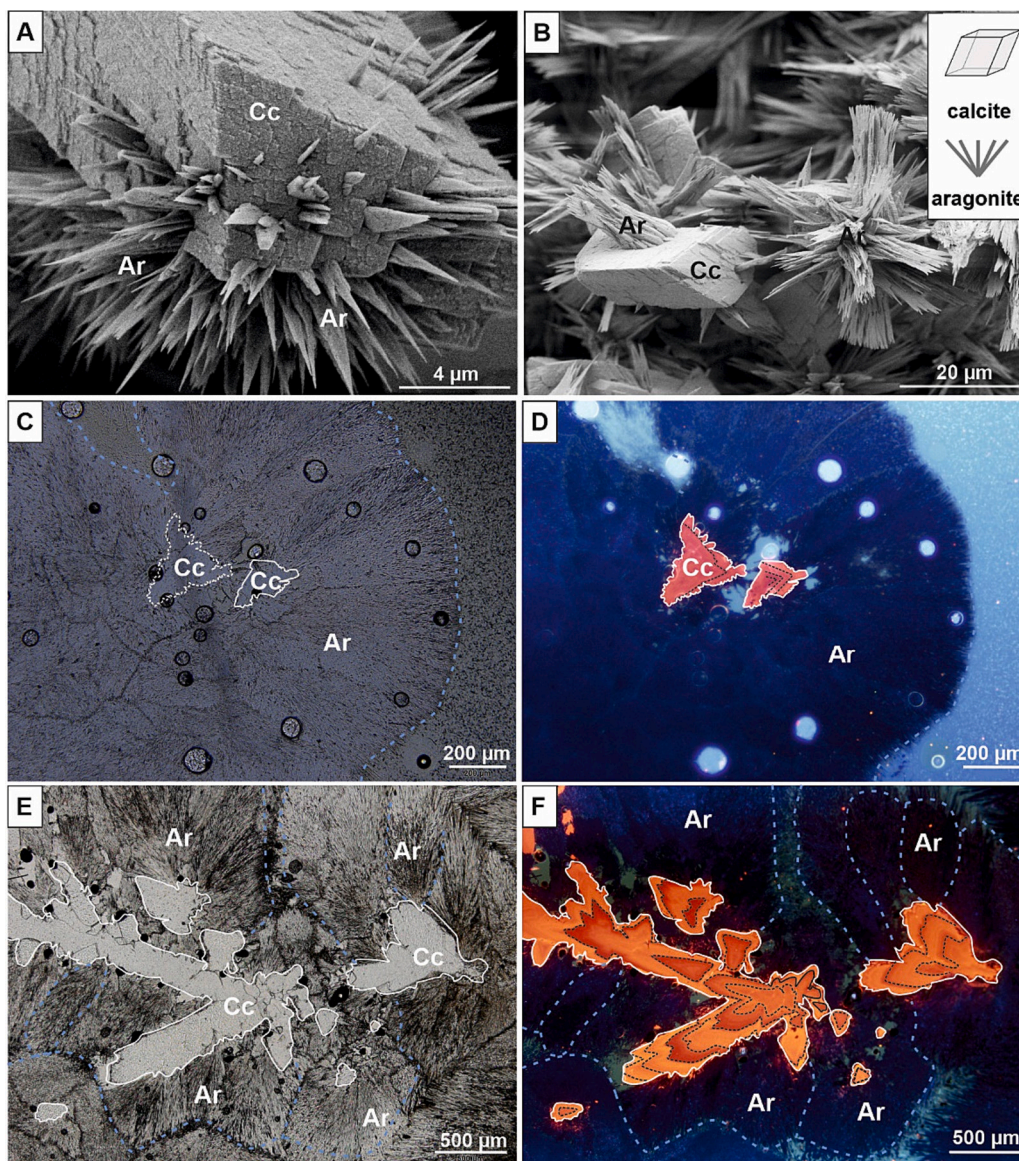


Fig. 3. SE-SEM images of the sample “Erz” (A–B) showing acicular aragonite crystals growing outwards from rhombohedral calcite crystals. CL images (C–F) of cross-sections of the same sample illustrating the growth relationship of aragonite and calcite. The calcite crystals (Cc) reveal uni- to bidirectional and rhombohedral to triangular growth patterns. Calcite zonation is locally disturbed by the onset of aragonite crystallization (Ar).

indicate the occurrence of narrow rims of HMC in the course of the successive evolution of the CaCO_3 polymorphism.

4.1.4. Field experiments

The sample holders were exposed to the sinter basin fluid in order to analyze the current hydrochemical state and ongoing formation of aragonite and calcite (Fig. 5A). After one week of exposure to the CaCO_3 supersaturated fluids, the sample holders containing the substrates were recovered from the sinter basin and analyzed under the SEM (Fig. 5B – 5E). The SEM images clearly confirm the repeated sequence of calcite and aragonite, with aragonite crystals being only detected on newly formed calcite crystals. Exposed rhombohedral calcite seed crystals show newly grown, smaller LMC crystals on the seed surface, followed by aragonite precipitation at available surface sites thereof (Fig. 5D & 5E). The newly grown calcite crystals are trigonal-rhombohedral in morphology with a prominently stepped surface in most of the cases. The exposed aragonite seed crystals reveal the same sequence of newly formed calcite initially followed by another generation of aragonite crystals. All of the detected newly formed aragonite crystals are grown

on newly formed LMC crystals (Fig. 5B & 5C). Thus, preferential nucleation and crystal growth of aragonite on the extent of primary/secondary calcite surfaces progressed regardless of the pristine seed crystal mineralogy. Also, the observed newly formed aragonite and calcite crystals are significantly smaller (up to 10 μm in size) than the underlying seed crystals ($\sim 30 \mu\text{m}$).

4.2. Geochemical composition of the aqueous solutions

The monitoring probes revealed low fluid temperatures from 4.3 to 5.6 $^\circ\text{C}$ in the sinter basin. The relative humidity ranged from 89 to 100%, the air temperature varied between 3.7 and 5.5 $^\circ\text{C}$ and the concentration of CO_2 was highly variable in the concentration range from 4700 to 10,000 ppm, whereby 10,000 ppm represents the upper technical measurement limit of the data logger applied (Fig. 6A & 6B and Fig. A.1 in the Appendix).

Water chemistry parameters of the inflowing fluid from the borehole and the sinter basin (Table 1; Fig. 6) document a high variability between the individual sampling campaigns and a strong differentiation

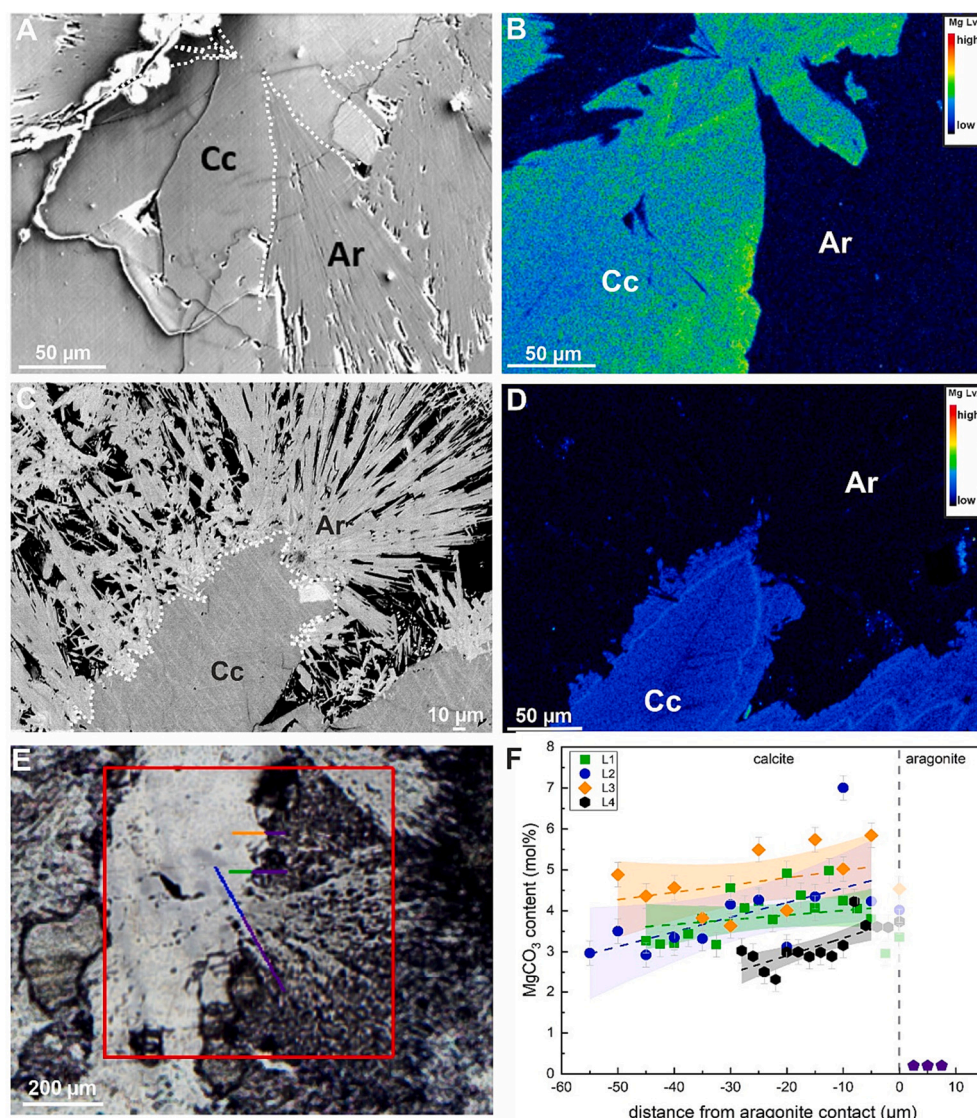


Fig. 4. BSE images and elemental distribution maps of Mg obtained from the sample “Erz”. A, C and E show intergrowth features of calcite and aragonite at different magnifications. B, D and F reveal the Mg distribution from the areas shown in A, C and E. The EMPA analyses confirm that most of the aragonite crystals grow from a mature calcite substrate already having a significantly elevated Mg content compared to the initial core regions of the crystals. E & F: Compilation of Raman spectroscopic observations. E) Positions of the line scans (line L1: green, line L2: blue, line L3: orange) are indicated and intersect with the calcite-aragonite interface. Note that line L4 (black symbols in F) lies outside of the shown area. Purple segments mark measurements of aragonite. F) Increasing MgCO_3 content (mol%) within calcite with decreasing distance to the aragonite grain boundary. The lighter-colored symbols mark the interface area between aragonite and calcite, where a mixed signal cannot be excluded due to the spot size ($<2 \mu\text{m}$) and the 3D geometry of the individual crystals. Note that the MgCO_3 content of aragonite lies between 0.02 and 0.20 mol% and is shown as purple line segments in E close to the calcite aragonite transition. (For interpretation of the references to colour in this figure legend, the reader is referred to the web version of this article.)

between the two locations regarding pH, alkalinity and the dominant ion concentrations, such as Ca^{2+} and Mg^{2+} . All of the investigated solutions reveal pH values ranging from 7.12 to 8.14, which are systematically lower than the pH values known from the Erzberg vein drainages, i.e., seepage water collected from fractures accessible at the surface of Erzberg (Boch et al., 2019). The SpC values of the aqueous solutions from the borehole revealed a systematically higher mineralization than the solutions from the sinter basin. The fluid temperatures of the borehole and sinter basin waters were consistently low (4.3 to 6.5 °C) during the monitoring period, whereas the alkalinity (given as HCO_3^-) was high throughout (590 to 788 mg/L). The concentrations of Mg^{2+} (78 to 106 mg/L) and Ca^{2+} (86 to 109 mg/L) ions also remained at a high level within the timeframe of observation. Thus, the solutions exhibited molar $\text{Mg}^{2+}/\text{Ca}^{2+}$ ratios from 1.4 to 1.8, with the lower values always seen in the fluids from the borehole and the higher ones analyzed in the sinter

basin. The molar $\text{Mg}^{2+}/\text{Ca}^{2+}$ ratios measured in the pore fluids expressed from the sample “Erz” are much higher compared to the bulk solutions, ranging from 2.9 to 3.8. Further, the K^+ and Na^+ concentrations show low values ranging from 0.3 to 2.7 mg/L and 0.7 to 2 mg/L, respectively. The SO_4^{2-} and Cl^- concentrations range from 42 to 54 mg/L and 1.4 to 3.1 mg/L, respectively. The dissolved $\text{Si}(\text{OH})_4$ concentrations amount to 4.2 up to 38.4 mg/L. *minor* and trace element concentrations in the solutions, including Al, Ba, Sr and Fe, were highly variable but inconspicuous among the sampling sites (see Table 1). The stable isotopic compositions of the investigated solution ($n = 1$) were determined as -74.6‰ and -10.77‰ VSMOW for $\delta^2\text{H}$ and $\delta^{18}\text{O}$, respectively. The inflowing water volume revealed some variability in a range from 3 to 5.2 mL/s (Table 2).

The SI values of the aqueous solutions with respect to the CaCO_3 polymorphs mostly reveal supersaturation or close to saturation states

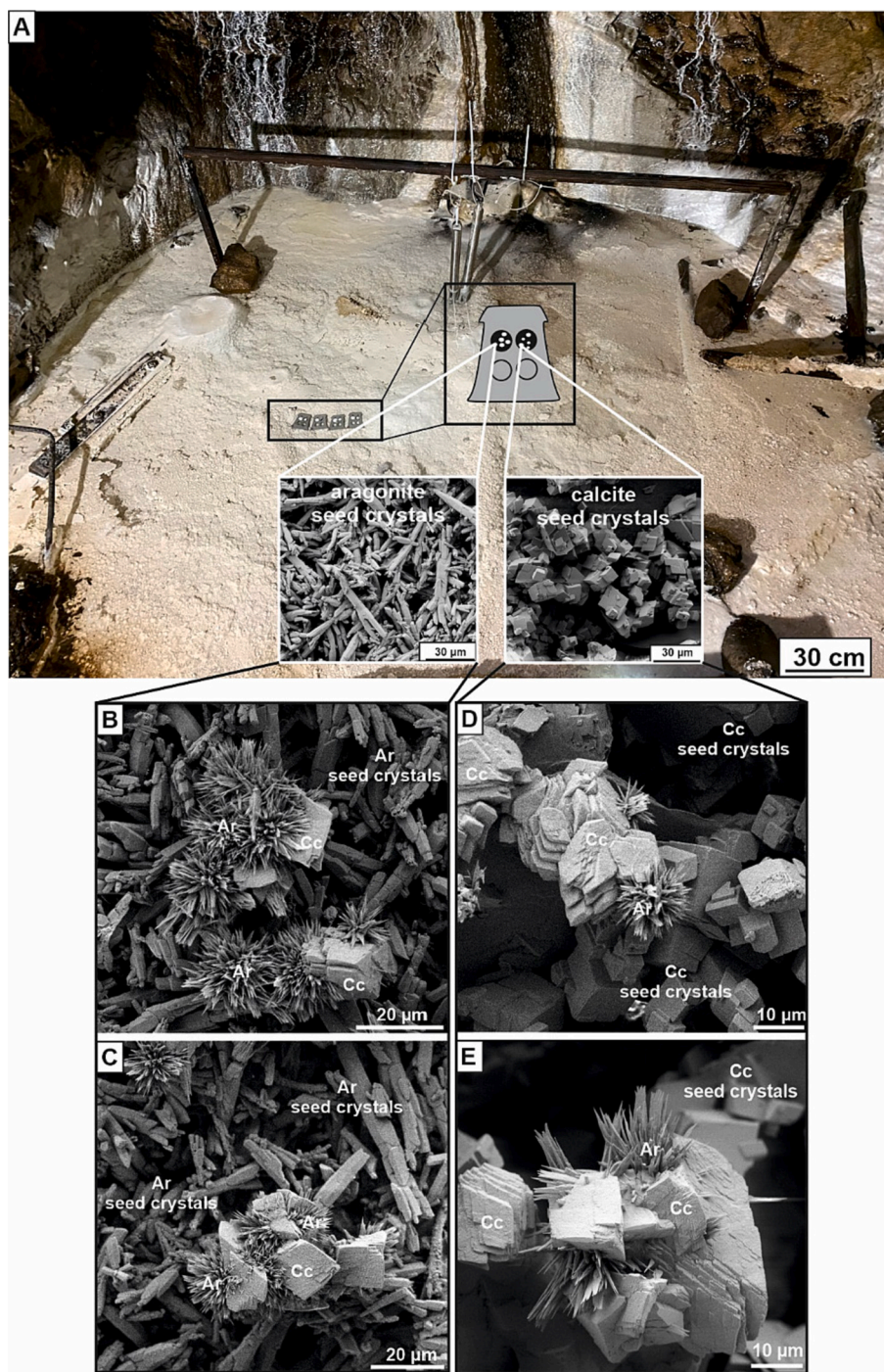


Fig. 5. Set-up and microscopic appearance of calcite-aragonite intergrowths obtained from a field experiment resembling the formation conditions of sample “Erz”. Sample holders with predetermined seed crystals of either aragonite or calcite were placed in the central part of the sinter basin (A). SE-SEM images showing the aragonite (B & C) and calcite (D & E) seed crystals after one week of exposure to the CaCO_3 supersaturated water. The newly formed aragonite (Ar) and calcite (Cc) crystals are smaller than the exposed seed crystals and exhibit acicular (Ar) and rhombohedral to skalenohedral crystal shapes (Cc), respectively, rather similar to sample “Erz”.

for calcite (0.0 to 1.0), aragonite (−0.2 to 0.8) and vaterite (−0.6 to 0.4), whereas ACC and ikaite are always undersaturated and dolomite is strongly supersaturated in all solutions ($\text{SI} \leq 2.1$; Table 2). The modelled pCO_2 yields prominently high values, ranging from $10^{2.5}$ to $10^{-1.5}$ atm (3162 to 31,623 ppm CO_2), compared to Earth’s surface atmospheric values ($\sim 10^{-3.4}$ atm or 400 ppm CO_2). Calculated charge balance errors (CBE) are consistently below 5% in the investigated solutions.

5. Discussion

5.1. Hydrochemical evolution

5.1.1. Spatiotemporal evolution of seepage fluids

Modern aqueous solutions draining the Erzberg host rock in the vicinity of the open pit mine can be assigned to differentiated sections based on their distinct hydrochemical compositions (Fig. 1A). According to Boch et al. (2019), the northern, central and southern sections are

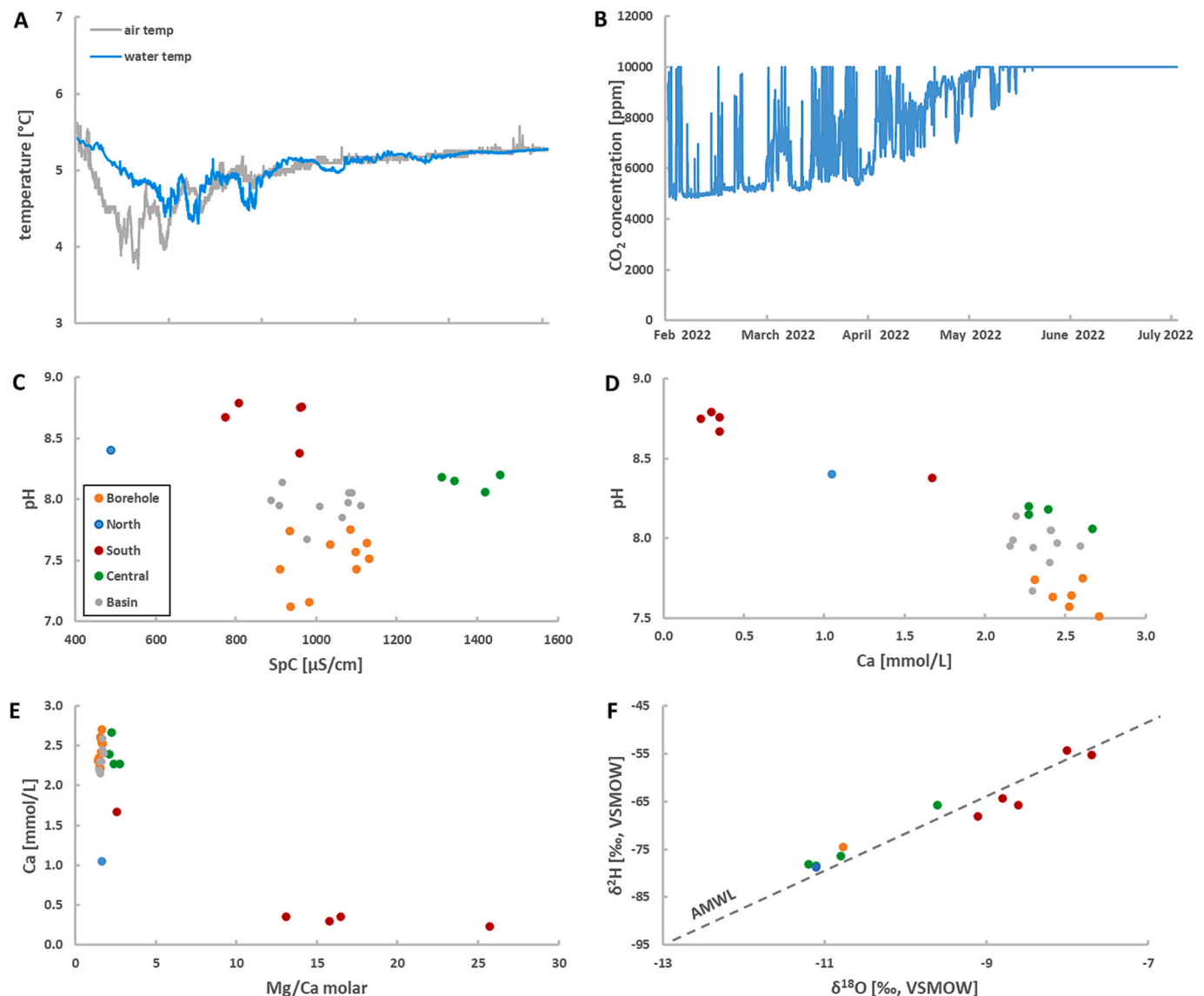


Fig. 6. Binary diagrams illustrating the hydrochemical relationships of spatially differentiated meteoric waters from Erzberg. Distinct differences between southern, central, and northern sampling sites (locations are marked in Fig. 1; data from Boch et al., 2019) and the investigated historic mining adit (fluid collected from the borehole and sinter basin) are evident. See text for explanation.

characterized by distinct water types Mg-Ca-HCO₃, Mg-Ca-HCO₃-SO₄ and Mg-HCO₃, respectively. The investigated seepage fluids from the borehole and the sinter basin from the studied subsurface adit site are located in the upper south-western part of the Erzberg mine, which corresponds to the southern section of the aforementioned classification (Fig. 1). However, the fluids represent a Mg-Ca-HCO₃ water type, which is closer to fluids known from the northern part of Erzberg. A possible explanation could be that the fluids are primarily sourced from the geographically upper part of the Erzberg mountain range, where Ca²⁺ is not yet consumed by successive CaCO₃ precipitation (e.g. as calcite and aragonite = erzbergite) along open fracture zones in the geographically deeper placed parts of Erzberg. This assertion is supported by the overall higher Ca²⁺ concentrations in the recently measured fluids compared to the seepage fluids collected from surface-exposed veins and fractures by Boch et al. (Boch et al., 2019; Fig. 6E).

Accordingly, the solutions draining the southern part of Erzberg mostly yielded higher pH values due to enhanced CO₂ degassing along the water flow path, corresponding decreased Ca²⁺ concentrations resulting from pronounced prior CaCO₃ precipitation (PCP) and thus, strongly increased molar Mg/Ca ratios (up to 26) compared to the

northern or central parts of Erzberg. The subsurface fluids from the investigated borehole and sinter basin reflect the overall composition of the central part although they are located in the more southern area of Erzberg (Fig. 1A & 6). Thus, these fluids reveal higher Ca²⁺ concentrations and lower pH values, as well as slightly lower molar Mg/Ca ratios, which can be attributed to the beginning of the meteoric water infiltration into the joints and fracture zones where CO₂ degassing and consequently (prior) CaCO₃ formation is yet less developed compared to the southern Erzberg area where most of the erzbergite (aragonite-calcite) fracture fillings were found (cf. Boch et al., 2019). The relatively constant but elevated aqueous molar Mg/Ca ratio indicates some incongruent Mg-rich host rock dissolution (e.g. dolomite or dolomitized limestone; Hanshaw and Back, 1979; Boch et al., 2019).

The δ²H and δ¹⁸O values of the fluid from the sinter basin reveal a meteoric origin with a lower H versus O isotopic distribution closer to the Austrian Meteoric Water Line (AMWL in Fig. 6F; cf. Hager and Foelsche, 2015) compared to the typical southern section fluids. This suggests a higher elevation of the principal meteoric water infiltration area, typically reflecting fluids from the central and northern part of Erzberg. This observation indicates that the location of the herein

Table 1

Summary of the water parameters measured at the sampling site, Zentrum am Berg, Erzberg (Austria). Reported are pH, T = temperature, SpC = specific electric conductivity, alkalinity (reported as HCO₃⁻), and the concentrations of major and minor solutes. During 10 sampling campaigns over 15 months water samples of a sinter basin and borehole were obtained (see Fig. 1 for sampling locations).

Sample ID	Date	T	pH	SpC	HCO ₃	Ca	Mg	Mg/ Ca	Na	K	Cl	SO ₄	Si (OH) ₄	Al	Ba	Fe	Sr
		(°C)		(µS/ cm)	mg/l	[mg/ l]	[mg/ l]	molar	[mg/ l]	[mg/ l]	[mg/ l]	[mg/ l]	[mg/ l]	[µg/ l]	[µg/ l]	[µg/ l]	[µg/ l]
Erz_basin_1	17.06.2021	5.6	7.94	1008	673	92	93	1.7	1.0	0.6	1.7	43	5	63	10	9	54
Erz_borehole_1	17.06.2021	5.6	7.63	1034	698	97	93	1.6	1.2	0.7	1.9	42	5	62	9	7	53
Erz_basin_2	24.11.2021	5.5	7.97	1079	696	98	100	1.7	1.2	0.6	2.1	52	5	62	9	< 1	57
Erz_borehole_2	24.11.2021	5.5	7.43	1100	714	104	100	1.6	1.2	0.7	2.1	52	5	62	10	< 1	57
Erz_basin_3	22.02.2022	5.5	7.85	1065	710	96	100	1.7	0.9	0.4	1.7	53	5	80	9	20	53
Erz_borehole_3	22.02.2022	6.1	7.75	1085	727	105	99	1.6	1.1	0.5	1.9	53	5	81	10	23	57
Erz_basin_4	01.03.2022	5.2	7.95	1110	762	104	106	1.7	0.9	0.4	1.8	55	5	64	11	< 1	58
Erz_borehole_4	01.03.2022	5.5	7.51	1132	788	109	106	1.6	1.3	1.0	1.9	55	5	66	11	< 1	61
Erz_basin_5	09.03.2022	4.9	8.05	1089	743	97	102	1.7	1.0	0.4	1.9	50	5	56	9	2	53
Erz_borehole_5	09.03.2022	5.5	7.64	1126	760	102	102	1.6	1.1	1.3	2.6	50	5	68	10	3	59
Erz_basin_6	16.03.2022	5.2	8.05	1082	732	96	104	1.8	1.0	0.4	2.0	49	5	60	10	< 1	54
Erz_borehole_6	16.03.2022	5.9	7.57	1098	744	101	103	1.7	1.2	0.7	2.2	49	6	58	10	3	57
Erz_basin_7	19.04.2022	6.2	7.95	908	611	86	82	1.6	0.7	0.3	1.3	46	5	62	10	23	50
Erz_borehole_7	19.04.2022	6.1	7.12	937	604	89	82	1.5	1.0	2.2	3.1	46	4	58	12	< 1	51
Erz_basin_8	23.04.2022	6.3	7.99	888	631	87	82	1.6	0.8	0.4	1.4	46	4	54	10	< 1	49
Erz_borehole_8	23.04.2022	6.5	7.43	910	630	90	81	1.5	0.9	2.7	3.9	46	4	55	9	26	51
Erz_basin_9	18.05.2022	5.4	8.14	916	590	88	78	1.5	2.0	1.6	1.7	45	4	50	8	< 1	44
Erz_borehole_9	18.05.2022	6.0	7.74	935	607	93	78	1.4	0.9	1.0	2.0	44	4	58	7	11	48
Erz_basin_10	27.09.2022	5.5	7.67	977	649	92	85	1.5	1.0	0.5	1.6	54	4	63	12	4	53
Erz_borehole_10	27.09.2022	5.8	7.16	983	654	94	84	1.5	1.0	0.7	1.9	54	38	68	13	2	55

Table 2

Measured and modelled hydrochemical parameters that correspond to the water samples of the sinter basin and borehole at the sampling site, Zentrum am Berg, Erzberg (Austria) for each sampling campaign ($n = 10$; labelled 1 to 10), including charge balance error (CBE), mineral saturation indices (SI) for calcite, aragonite, vaterite, amorphous CaCO₃ (ACC), ikaite and dolomite, internal partial pressure of CO₂ (logP_{CO2}) and water flow rate (Q).

Sample ID	Date	logP _{CO2} atm.	SI _{calcite}	SI _{aragonite}	SI _{vaterite}	SI _{Acc}	SI _{ikaite}	SI _{dolomite}	CBE %	Q mL/s
Erz_basin_1	17.06.2021	-2.3	0.9	0.7	0.3	-1.7	-0.5	1.8	1.3	
Erz_borehole_1	17.06.2021	-1.9	0.6	0.4	0.0	-2.0	-0.8	1.2	0.7	5.2
Erz_basin_2	24.11.2021	-2.3	0.9	0.8	0.4	-1.7	-0.5	1.9	2.5	
Erz_borehole_2	24.11.2021	-1.7	0.4	0.3	-0.2	-2.2	-0.9	0.9	2.5	4.9
Erz_basin_3	22.02.2022	-2.2	0.8	0.6	0.2	-1.8	-0.6	1.7	1.3	
Erz_borehole_3	22.02.2022	-2.1	0.8	0.6	0.2	-1.8	-0.6	1.6	1.5	4.8
Erz_basin_4	01.03.2022	-2.3	1.0	0.8	0.4	-1.7	-0.4	2.0	0.7	
Erz_borehole_4	01.03.2022	-1.8	0.6	0.4	0.0	-2.1	-0.8	1.2	0.3	4.8
Erz_basin_5	09.03.2022	-2.4	1.0	0.8	0.4	-1.6	-0.4	2.1	0.0	
Erz_borehole_5	09.03.2022	-1.9	0.7	0.5	0.1	-1.9	-0.7	1.4	-0.2	3.6
Erz_basin_6	16.03.2022	-2.4	1.0	0.8	0.4	-1.6	-0.4	2.1	1.3	
Erz_borehole_6	16.03.2022	-1.9	0.6	0.4	0.0	-2.0	-0.8	1.3	1.2	3.0
Erz_basin_7	19.04.2022	-2.3	0.8	0.6	0.3	-1.8	-0.6	1.7	0.4	
Erz_borehole_7	19.04.2022	-1.5	0.0	-0.2	-0.6	-2.6	-1.4	0.1	1.4	4.9
Erz_basin_8	23.04.2022	-2.4	0.9	0.7	0.3	-1.7	-0.5	1.9	-1.1	
Erz_borehole_8	23.04.2022	-1.8	0.4	0.2	-0.2	-2.3	-1.0	0.7	-0.9	4.6
Erz_basin_9	18.05.2022	-2.5	1.0	0.8	0.4	-1.6	-0.4	2.0	1.4	
Erz_borehole_9	18.05.2022	-2.1	0.7	0.5	0.1	-1.9	-0.7	1.3	1.1	3.6
Erz_basin_10	27.09.2022	-2.0	0.6	0.4	0.0	-2.0	-0.8	1.2	-0.7	
Erz_borehole_10	27.09.2022	-1.5	0.1	-0.1	-0.5	-2.5	-1.3	0.2	-0.9	4.4

studied fluid sample is geographically significantly elevated compared to the southerly located fluids (Boch et al., 2019; Fig. 1A). In essence, our new data support the current hypothesis explaining the hydrochemical evolution of seepage fluids and the closely related precipitation of Ca-(Mg)-carbonate (e.g. erzbergite, authigenic dolomite) at Erzberg (cf., Boch et al., 2019; Baldermann et al., 2020). In all of these new studies dealing with secondary Ca-(Mg)-carbonate precipitates in fractures and in the subsurface of Erzberg the occurrence of LMC, HMC and aragonite was found and HMC is always of minor relevance with respect to the amount, i.e. representing an intermediate stage in the course of the calcite to aragonite evolution from the vadose fluids.

5.1.2. Effect of environmental change on aqueous solution composition

The hydrochemical composition of the fluids from the studied

underground area reveals some distinct spatial differences. Fluids from the borehole yielded higher SpC values and higher Ca²⁺ concentrations at lower pH values compared to the fluids from the adjacent sinter basin (Table 1). The Mg²⁺ concentration is similar at both sampling locations, but minor differences are seen between the individual sampling campaigns, probably reflecting some seasonal influences. Observed lower SpC and Ca²⁺ values at higher pH in the sinter basin fluids likely result from pronounced in-situ CaCO₃ precipitation according to the overall reaction:



This assumption is also supported by systematically lower pCO₂ values in solutions from the sinter basin compared to those from the borehole (Fig. 7A; Table 2). Thus, degassing of CO₂ represents the main driving mechanism for calcite and aragonite supersaturation and

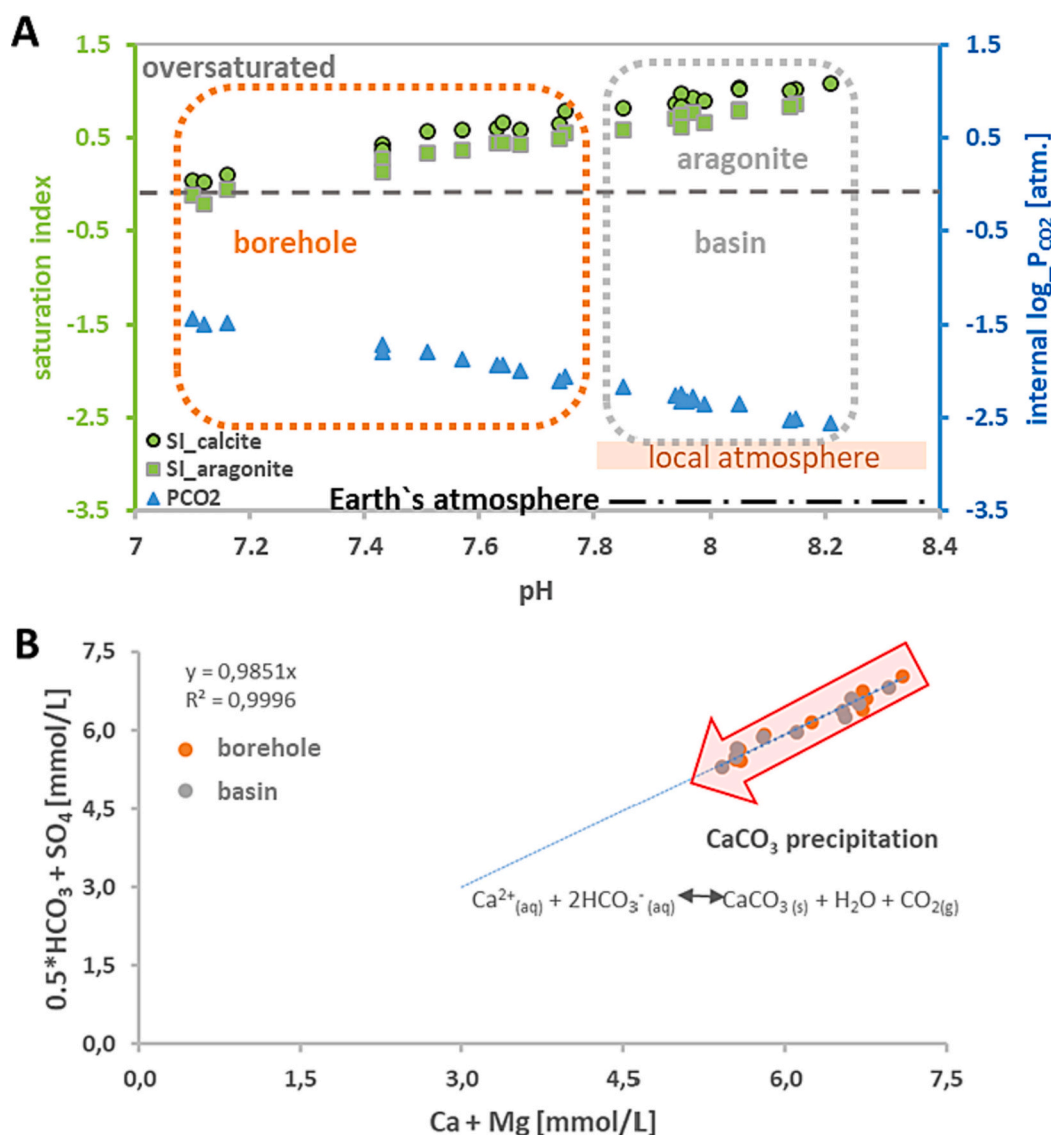


Fig. 7. (A) Modelled data (input: chemical composition of aqueous solutions collected from the borehole and the sinter basin between May 2021 and September 2022) illustrating that degassing of CO₂ from the solution is the driving mechanism for calcite and aragonite supersaturation and precipitation. (B) Plot of the molar Ca + Mg concentration versus the concentration of HCO₃ (≈DIC at 6.3 < pH < 8.3) + SO₄ of all analyzed samples. The slope of the linear regression line of ~1 indicates a decrease of the Ca and HCO₃ concentration due to precipitation of CaCO₃ minerals (red arrow). (For interpretation of the references to colour in this figure legend, the reader is referred to the web version of this article.)

ongoing CaCO₃ precipitation in the sinter basin (Fig. 7A; Table 2), since degassing of CO₂ increases the pH value and the DIC content of the solution (Plummer and Busenberg, 1982). The successive precipitation of CaCO₃ minerals further results in a significant loss of Ca²⁺, Mg²⁺ and CO₃²⁻ ions (Fig. 7B, red arrow), which also leads to a decrease in the SpC of the sinter basin (Hayashi, 2004; Table 1).

Distinct temporal changes in the hydrochemistry of the sinter basin were observed, which are probably caused by seasonal environmental change. We suggest that the water discharge from the borehole to the sinter basin had an important influence on the hydrochemical evolution of the solutions and the related mineral deposits in the sinter basin. The fluid temperature was found to decrease with decreasing discharge from the borehole, suggesting that the fluid temperature is strongly controlled by the prevalent air temperature in the historic adit. For example, the air temperature of the mine system decreased in March 2022 (see Fig. 6A) due to blowing snow and freezing temperatures outside the subsurface mining site at this time. The shift of the air temperature also corresponds well to changes in the overall pCO₂ level and in relative humidity

(Fig. 6B and Fig. A.1; Appendix), since cold air can absorb less moisture (Kim et al., 2018). The continuously logged data show that a colder air flow prevailed in the historic tunnel system at the beginning of March 2022, which presumably led to increased CO₂ degassing and thus to increased CaCO₃ supersaturation and precipitation in the sinter basin. This assumption is supported by decreasing SpC values and slightly increasing pH values, as well as the molar Mg/Ca ratios at this time (Table 1). The overall mineralization degree of the sinter basin solution decreased due to the enhanced removal of major ions (e.g. Ca²⁺) and the precipitation of CaCO₃ minerals, which subsequently resulted in an overall increase of the aqueous Mg/Ca ratio, as Mg is barely incorporated into the calcite crystal lattice and is virtually absent in aragonite (Huang and Fairchild, 2001; Riechelmann et al., 2014; Boch et al., 2019). The pH increase of the solution also suggests enhanced CO₂ degassing (removal of carbonic acid) as the main CaCO₃ formation process, which also indicates that the historic adit is well connected to the outside atmosphere and to the pronounced seasonal environmental change at the surface. Modern CaCO₃ samples, however, were not

collected continuously (i.e. natural samples only in the beginning of the monitoring period and crystals on artificial substrates later during one sampling campaign) and systematic changes in the solid sample amounts and compositions related to atmospheric CO₂ variations were therefore not investigated. From the various parameters monitored a major relation of CaCO₃ precipitation and the related polymorphism to the air vs. aqueous CO₂ dynamics seems obvious and support other data and interpretations from Erzberg (Boch et al., 2019; Baldermann et al., 2020).

5.2. Controls on calcite – Aragonite growth sequences

The recurrent deposition of unique aragonite and calcite sequences seems to be a characteristic feature of the historic subsurface adit at Erzberg (Fig. 2). Calcite and aragonite occur in variable proportions across the investigated sample “Erz” with the aragonite content increasing towards the bottom and top of the sample (Fig. 2A). The bottom side of the sample mainly consists of spherical structures made of an inner core of calcite, which is surrounded by bundles of acicular aragonite crystals (Fig. 2 - 4). Identical growth patterns have been observed upon exposure of predefined calcite and aragonite seed crystals in the sinter basin for one week duration only (Fig. 5). Interestingly, the newly formed aragonite crystals precipitated only on newly formed

calcite surfaces, suggesting that their occurrence is causally linked to the initial growth of calcite crystals (Fig. 8). Thus, the distinct mineralogy of the seed crystals does not take control on the subsequent precipitation of certain CaCO₃ polymorphs from the supersaturated Erzberg waters. This atypical observation can be explained by PCP, which increased the aqueous Mg²⁺/Ca²⁺ ratio in the sinter basin (Fig. 8; Fairchild et al., 2000; Boch et al., 2019; Riechelmann et al., 2014). The ratio of Mg²⁺ to Ca²⁺ ions in solution in low temperature settings is known to be a key driver for determining calcite-aragonite polymorphism (Morse et al., 1997 & Morse et al., 2007).

Calcite incorporates variable amounts of Mg²⁺ ions in the crystal lattice to form LMC and subsequently – at a certain aqueous Mg/Ca ratio – HMC (Fig. 4B and Fig. 8). This discriminated Mg content in calcite is causing the aqueous Mg²⁺/Ca²⁺ ratio to increase during ongoing calcite precipitation, in particular if the water discharge is reduced until the precipitation of aragonite occurs (Morse et al., 2007). Adsorption of Mg²⁺ ions to calcite growth sites inhibits an undisturbed, gradual progression, slowing down the overall growth rate of calcite due to Mg poisoning of the calcite growth surface (Fig. 8). Thus, elevated Mg/Ca ratios of the seepage fluids at Erzberg generally promote aragonite instead of calcite nucleation (Reddy and Wang, 1980; Astilleros et al., 2010; Riechelmann et al., 2014; Rossi and Lozano, 2016; Purgstaller et al., 2017) above some critical aqueous Mg/Ca limit (Rodriguez-

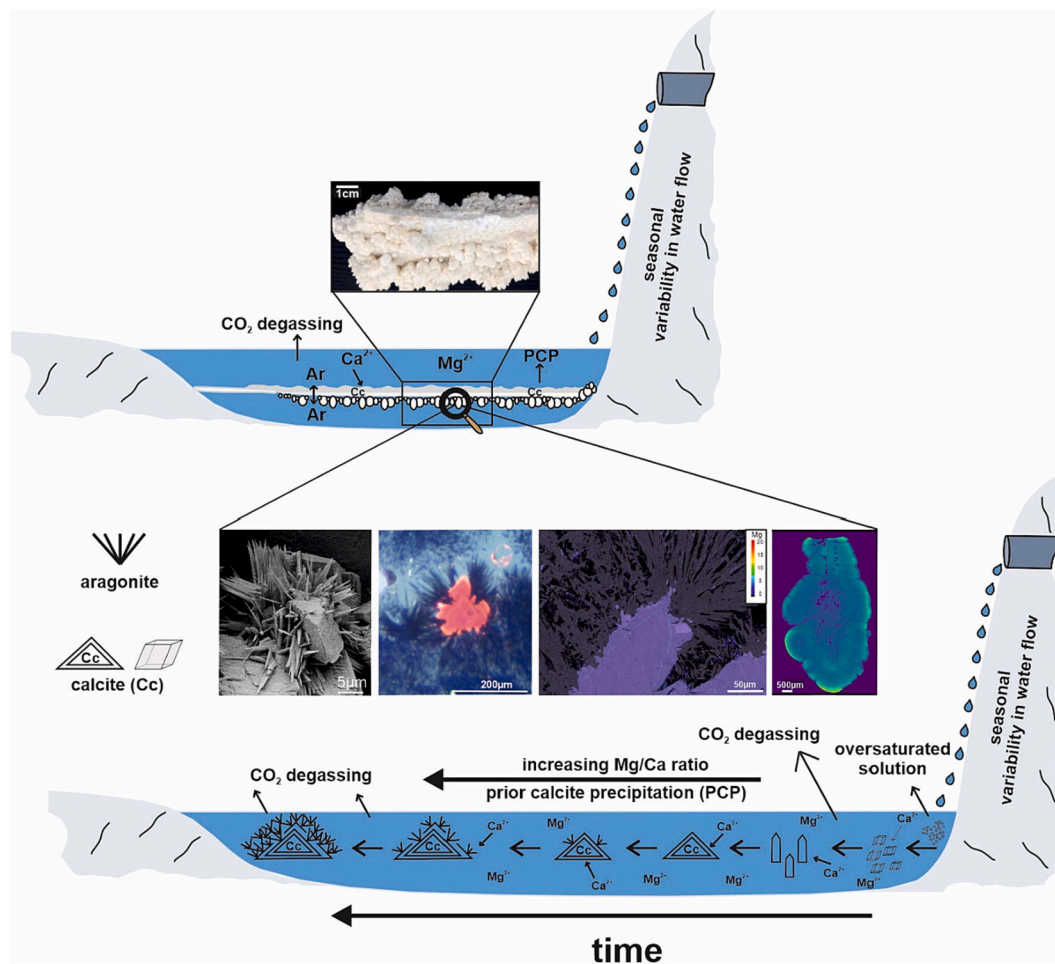


Fig. 8. Schematic illustration of the chemical reaction mechanisms occurring in the sinter basin of the subsurface site at Erzberg. The seasonal variability of the incoming water flow and the prevailing water volume in the sinter basin influence the hydrochemistry and thus the aqueous molar Mg/Ca ratio in the sinter basin. Enhanced degassing of CO₂ to the surrounding atmosphere (adit) provides an increasingly supersaturated solution with respect to calcite and aragonite, from which low-Mg calcite crystals precipitate first. With ongoing prior calcite precipitation (PCP), the aqueous molar Mg/Ca ratio increases progressively, causing high-Mg calcite to form locally until the precipitation of aragonite crystals occurs. Aragonite crystals further grow simultaneously with calcite crystals for a short time period until the aqueous molar Mg/Ca ratio is high enough to prevent any further Mg-calcite nucleation and growth. Distinct idiomorphic morphologies and crystal shapes reflect the successive hydrochemical evolution and interrelated CaCO₃ polymorphism.

Navarro and Benning, 2013; Casella et al., 2017; Boch et al., 2019). This threshold is known to be between 1 and 3 for aqueous molar Mg/Ca ratios (Frisia et al., 2002; Dietzel et al., 2004) and overlaps with the measured Erzberg fluid compositions (molar Mg/Ca ratios range from 1.5 to 1.8; Table 1).

The aqueous molar Mg^{2+}/Ca^{2+} ratios of the fluids from the sinter basin likely depended on changes in the water inflow and thus on seasonal environmental changes, as the highest Mg^{2+}/Ca^{2+} values of 1.8 correspond well to the lowest water discharge of 3 mL/s, predefining the formation of calcite and/or aragonite layers/spherules (Fig. 8). The relevance of variable water inflow and hence water level fluctuations in the sinter basin is also expressed in the morphology of the calcite-aragonite successions (cf. “layers” of sample Erz11). Detailed petrographic analyses indicate that aragonite crystals started to nucleate preferentially from existing growth sites hosting an elevated Mg concentration in the calcite structure. In some cases, the predominant LMC (~3.1 mol% $MgCO_3$) changed to a HMC (~4.8 mol% $MgCO_3$) due to progressive isomorphous substitution of Mg^{2+} for Ca^{2+} in the crystal structure of calcite (Busenberg and Plummer, 1989), i.e., before the aragonite crystals started to grow (Fig. 4B & 4D). Such inhibition of calcite nucleation upon Mg^{2+} uptake is primarily due to an increase in surface energy (Sun et al., 2015), which is not the case for aragonite, as this phase does not incorporate significant Mg contents into the crystal lattice (Morse et al., 2007). Magnesium incorporation into calcite, however, results in some distortion of its structure (small ionic radius of Mg^{2+}) and the solubility of calcite consequently increases with increasing solid Mg content; note that LMC with 4 mol% $MgCO_3$ is the thermodynamically most stable, least soluble Mg calcite phase (Busenberg and Plummer, 1989; Davis et al., 2000).

As a result, thermodynamically metastable aragonite can become the predominant $CaCO_3$ polymorph, which suppresses the steady-state nucleation rate of calcite and subsequently grows preferentially from Mg enriched calcite growth surfaces (Fig. 4 E & 4F; Baumgartner et al., 2013; Sun et al., 2015). Boon et al. (2020) deduced aragonite nucleation to be induced at disordered nucleation sites via a kind of amorphous Mg-Ca carbonate precursor structure. However, the disturbed zonation in the calcite crystals suggests that calcite also continues to grow together with aragonite for a short time period (Fig. 4), i.e. until the molar Mg/Ca ratio in the solution is high enough to inhibit any formation and growth of calcite, giving rise to the dominance of aragonite (Lippmann, 1973; Berner, 1975; Fernández-Díaz et al., 1996; De Choudens-Sanchez and Gonzalez, 2009). The herein documented calcite-aragonite evolution at Erzberg at low temperature has important implications for the proxy signal development (i.e. trace element incorporation; stable isotopes of O and C) in growing $CaCO_3$ sequences, such as in speleothems. Wasenburger et al. (2016) have shown that aragonite precipitation can have a huge impact on the speleothem trace element records, favouring for instance U uptake over speleothem calcite, which has important implications for age dating. On the contrary, precipitation of metastable aragonite in calcite-dominated sedimentary records and its post-depositional recrystallization into calcite will disturb the pristine trace elemental and isotopic signals recorded in the $CaCO_3$ sequences. We therefore conclude that high-spatial resolution techniques should be applied to repeated $CaCO_3$ growth sequences in order to identify pristine versus secondary $CaCO_3$ precipitates.

6. Conclusions

The formation process of prominent calcite-aragonite mineral sequences deposited in a historical subsurface adit at Erzberg (Austria) in recent times (< 150 years) was investigated using a combination of (i) in-situ, time-resolved measurements of fluid and air temperature, relative humidity and atmospheric CO_2 concentration, (ii) bulk and high-resolution optical, mineralogical and chemical analytical tools (XRD, CL, Raman, SEM and EPMA) and (iii) field experiments applying artificial substrates and seed crystals in order to document the enigmatic

calcite-aragonite transition.

The formation of distinct $CaCO_3$ polymorphs can be explained by a combination of seasonal environmental change (air temperature and water discharge) and the closely related hydrochemical composition of the Erzberg seepage fluids, i.e., the lowest discharge correlated with the highest aqueous molar Mg/Ca ratio. Enhanced and prolonged degassing of CO_2 from the CO_2 -enriched seepage water into the atmosphere of the adit was identified as the main driver of pronounced $CaCO_3$ precipitation, causing high supersaturation of calcite and aragonite in the investigated sinter basin fluid. Field-based experiments utilizing either aragonite or calcite seeds indicate that LMC crystals always precipitate at first, followed by HMC zones, from which acicular shaped aragonite crystals started to nucleate, similar to the succession observed in the natural calcite-aragonite deposits of the sinter basin. We conclude that ongoing prior calcite precipitation caused an increase of the aqueous Mg/Ca ratio, so that the precipitating calcite crystals successively incorporated Mg to form LMC followed by HMC. This led to a higher nucleation surface energy and higher solubility of (Mg-)calcite, which allowed aragonite to grow selectively from the distorted calcite surfaces. Subsequently, the growth kinetics of metastable aragonite surpassed that of calcite once a certain aqueous molar Mg/Ca ratio in solution was reached (~1–2), marking the onset of the calcite-to-aragonite transition. Our observations reveal that formation of differentiated calcite-aragonite successions in sedimentary deposits require dynamic environmental changes and fluctuations in seepage water chemistry, which both take key control on $CaCO_3$ surface characteristics, precipitation mode and polymorphism.

Declaration of Competing Interest

The authors declare that they have no known competing financial interests or personal relationships that could have appeared to influence the work reported in this paper.

Data availability

Data will be made available on request.

Acknowledgements

Judith Jernej, Maria Hierz, Andrea Wolf and Sylvia Perchthold are acknowledged for their dedicated work in the IAG laboratories. We are grateful to Jennifer Pöttler for her previous work on the Erzberg samples. Chemical and mineralogical analyses were conducted in the NAWI Graz Central Lab for Water, Minerals and Rocks. We would also like to thank two anonymous reviewers and the editor Karen Johannesson for their evaluation and helpful comments to our manuscript.

Appendix A. Supplementary data

Supplementary data to this article can be found online at <https://doi.org/10.1016/j.chemgeo.2023.121768>.

References

- Arbeiter, F., Eichinger, S., Rieß, G., Schachinger, T., Boch, R., Wenighofer, R., Galler, R., Hausberger, A., Strobl, E., Stur, M., Saliger, F., Steiner, M., Dietzel, M., Pinter, G., 2019. Optimierte Polymer-Rohrwerkstoffe für effiziente Drainagesysteme in Tunnelbauwerken–PolyDrain. BHM Berg-und Hüttenmännische Monatshefte 164 (12), 545–551.
- Astilleros, J.M., Fernández-Díaz, L., Putnis, A., 2010. The role of magnesium in the growth of calcite: an AFM study. Chem. Geol. 271, 52–58.
- Baldermann, A., Mittermayr, F., Bernasconi, S.M., Dietzel, M., Grengg, C., Hippler, D., Kluge, T., Leis, A., Lin, K., Wang, X., Zünterl, A., Boch, R., 2020. Fracture dolomite as an archive of continental palaeo-environmental conditions. Commun. Earth Environ. 1 (1), 35.
- Baumgartner, J., Dey, A., Bomans, P.H., Le Coadou, C., Fratzl, P., Sommerdijk, N.A., Faivre, D., 2013. Nucleation and growth of magnetite from solution. Nat. Mater. 12 (4), 310–314.

- Berner, R.A., 1975. The role of magnesium in the crystal growth of calcite and aragonite from sea water. *Geochim. Cosmochim. Acta* 39 (4), 489–504.
- Bischoff, J.L., Fitzpatrick, J.A., Rosenbauer, R.J., 1993. The solubility and stabilization of ikaite ($\text{CaCO}_3 \cdot 6\text{H}_2\text{O}$) from 0 to 25 °C: environmental and paleoclimatic implications for thinitite tufa. *J. Geol.* 101 (1), 21–33.
- Boch, R., Wang, X., Kluge, T., Leis, A., Lin, K., Pluch, H., Mittermayr, F., Baldermann, A., Böttcher, M., Dietzel, M., 2019. Aragonite–calcite veins of the ‘Erzberg’ iron ore deposit (Austria): Environmental implications from young fractures. *Sedimentology* 66 (2), 604–635.
- Boch, R., Pilgerstorfer, T., Moritz, B., 2022. Reduction of scale formation by optimized drainage conditions—Insights from field testing. *Geomechan. Tunnel.* 15 (4), 371–391.
- Boon, M., Rickard, W.D.A., Rohl, A.L., Jones, F., 2020. Stabilization of Aragonite: Role of Mg^{2+} and Other Impurity Ions. *Cryst. Growth Des.* 20, 5006–5017.
- Borromeo, L., Zimmermann, U., Andò, S., Coletti, G., Bersani, D., Basso, D., Gentile, P., Schulz, B., Garzanti, E., 2017. Raman spectroscopy as a tool for magnesium estimation in Mg-calcite. *J. Raman Spectrosc.* 48 (7), 983–992.
- Böttcher, M.E., Dietzel, M., 2010. Metal-ion partitioning during low-temperature precipitation and dissolution of anhydrous carbonates and sulphates. *Europ. Mineral. Union Notes Mineral.* 10 (1), 139–187.
- Brečević, L., Nielsen, A.E., 1989. Solubility of amorphous calcium carbonate. *J. Cryst. Growth* 98 (3), 504–510.
- Busenberg, E., Plummer, L.N., 1989. Thermodynamics of magnesian calcite solid solutions at 25 °C and 1 atm total pressure. *Geochim. Cosmochim. Acta* 53, 1189–1208.
- Casella, L.A., Grieshaber, E., Yin, X., Ziegler, A., Mavromatis, V., Müller, D., Ritter, A., Hippler, D., Harper, E., Dietzel, M., Immenhauser, A., Schöne, B., Angiolini, L., Schmah, W.W., 2017. Experimental diagenesis: insights into aragonite to calcite transformation of *Arctica islandica* shells by hydrothermal treatment. *Biogeosciences* 14 (6), 1461–1492.
- Davis, K.J., Dove, P.M., De Yoreo, J.J., 2000. The role of Mg^{2+} as an impurity in calcite growth. *Science* 290 (5494), 1134–1137.
- De Choudens-Sanchez, V., Gonzalez, L.A., 2009. Calcite and aragonite precipitation under controlled instantaneous supersaturation: elucidating the role of CaCO_3 saturation state and Mg/Ca ratio on calcium carbonate polymorphism. *J. Sediment. Res.* 79, 363–376.
- Dietzel, M., Gussone, N., Eisenhauer, A., 2004. Co-precipitation of Sr^{2+} and Ba^{2+} with aragonite by membrane diffusion of CO_2 between 10 and 50 °C. *Chem. Geol.* 203 (1–2), 139–151.
- Dove, P.M., De Yoreo, J.J., Weiner, S., 2003. Biomineralization.
- Drake, H., Mathurin, F.A., Zack, T., Schäfer, T., Roberts, N.M.W., Whitehouse, M., Karlsson, A., Broman, C., Åström, M.E., 2018. Incorporation of metals into Calcite in a Deep Anoxic Granite Aquifer. *Environ. Sci. Technol.* 52, 493–502.
- Eichinger, S., Boch, R., Leis, A., Koraimann, G., Grengg, C., Domberger, G., Nachtebel, M., Schwab, C., Dietzel, M., 2020. Scale deposits in tunnel drainage systems—a study on fabrics and formation mechanisms. *Sci. Total Environ.* 718, 137140.
- Fairchild, I.J., Borsato, A., Tooth, A.F., Frisia, S., Hawkesworth, C.J., Huang, Y., McDermott, F., Spiro, B., 2000. Controls on trace element (Sr–Mg) compositions of carbonate cave waters: implications for speleothem climatic records. *Chem. Geol.* 166 (3–4), 255–269.
- Falini, G., Reggi, M., Fermani, S., Sparla, F., Goffredo, S., Dubinsky, Z., Levi, O., Dauphin, Y., Cuif, J.P., 2013. Control of aragonite deposition in colonial corals by intra-skeletal macromolecules. *J. Struct. Biol.* 183, 226–238.
- Fernández-Díaz, L., Putnis, A., Prieto, M., Putnis, C.V., 1996. The role of magnesium in the crystallization of calcite and aragonite in a porous medium. *J. Sediment. Res.* 66, 482–491.
- Frisia, S., Borsato, A., Fairchild, I.J., McDermott, F., Selmo, E.M., 2002. Aragonite–calcite relationships in speleothems (Grotte de Clamouse, France): Environment, fabrics, and carbonate geochemistry. *J. Sediment. Res.* 72 (5), 687–699.
- Froitzheim, N., Plasińska, D., Schuster, R., 2008. Alpine tectonics of the Alps and Western Carpathians. Chapter in Book: The Geology of Central Europe.
- Fyfe, W.S., Bischoff, J.L., Pray, L.C., Murray, R.C., 1965. The Calcite–Aragonite Problem. In: Dolomitization and Limestone Diagenesis. SEPM Society for Sedimentary Geology.
- Hager, B., Foelsche, U., 2015. Stable isotope composition of precipitation in Austria. *Austr. J. Earth Sci.* 108 (2), 2–13.
- Hanshaw, B.B., Back, W., 1979. Major geochemical processes in the evolution of carbonate–aquifer systems. *J. Hydrol.* 43 (1–4), 287–312.
- Hayashi, M., 2004. Temperature–electrical conductivity relation of water for environmental monitoring and geophysical data inversion. *Environ. Monit. Assess.* 96, 119–128.
- Hoffmann, R., Richter, D.K., Neuser, R.D., Jöns, N., Linzmeier, B.J., Lemanis, R.E., Füsseis, F., Immenhauser, A., 2016. Evidence for a composite organic–inorganic fabric of belemnite rostra: Implications for palaeoceanography and palaeoecology. *Sediment. Geol.* 341, 203–215.
- Huang, Y., Fairchild, I.J., 2001. Partitioning of Sr^{2+} and Mg^{2+} into calcite under karst-analogue experimental conditions. *Geochim. Cosmochim. Acta* 65 (1), 47–62.
- Jamieson, J.C., 1953. Phase equilibrium in the system calcite–aragonite. *J. Chem. Phys.* 21 (8), 1385–1390.
- Kim, H., Rao, S.R., Kapustin, E.A., Zhao, L., Yang, S., Yaghi, O.M., Wang, E.N., 2018. Adsorption-based atmospheric water harvesting device for arid climates. *Nat. Commun.* 9 (1), 1191.
- Lippmann, F., 1973. *Sedimentary Carbonate Minerals*. Springer, Berlin, p. 229.
- Lumsden, D.N., Chimahusky, J.S., 1980. Relationship between Dolomite Nonstoichiometry and Carbonate Facies Parameters. In: Zenger, D.H., Dunham, J.B., Ethington, R.L. (Eds.), *Concepts and Models of Dolomitization*, 28. Society of Economic Paleontologists and Mineralogists, Special Publication, pp. 123–137.
- Mavromatis, V., Goetschl, K.E., Grengg, C., Konrad, F., Purgstaller, B., Dietzel, M., 2018. Barium partitioning in calcite and aragonite as a function of growth rate. *Geochim. Cosmochim. Acta* 237, 65–78.
- Morse, J.W., Wang, Q., Tsio, M.Y., 1997. Influences of temperature and Mg:Ca ratio on CaCO_3 precipitates from seawater. *Geology* 25 (1), 85–87.
- Morse, J.W., Arvidson, R.S., Lüttge, A., 2007. Calcium carbonate formation and dissolution. *Chem. Rev.* 107 (2), 342–381.
- Parkhurst, D.L., Appelo, C.A.J., 2013. Description of input and examples for PHREEQC version 3—a computer program for speciation, batch-reaction, one-dimensional transport, and inverse geochemical calculations. *US Geol. Surv. Tech. Methods* 6 (A43), 497.
- Perdikouri, C., Kasiopas, A., Geisler, T., Schmidt, B.C., Putnis, A., 2011. Experimental study of the aragonite to calcite transition in aqueous solution. *Geochim. Cosmochim. Acta* 75, 6211–6224.
- Plummer, L.N., Busenberg, E., 1982. The solubilities of calcite, aragonite and vaterite in CO_2 - H_2O solutions between 0 and 90 °C, and an evaluation of the aqueous model for the system CaCO_3 - CO_2 - H_2O . *Geochim. Cosmochim. Acta* 46 (6), 1011–1040.
- Prochaska, W., 2012. Siderite and magnesite mineralizations in Palaeozoic strata of the Eastern Alps (Austria). *J. Alpine Geol.* 54, 309–322.
- Purgstaller, B., Dietzel, M., Baldermann, A., Mavromatis, V., 2017. Control of temperature and aqueous $\text{Mg}^{2+}/\text{Ca}^{2+}$ ratio on the (trans-)formation of ikaite. *Geochim. Cosmochim. Acta* 217, 128–143.
- Reddy, M.M., Wang, K.K., 1980. Crystallization of calcium carbonate in the presence of metal ions: I. Inhibition by magnesium ion at pH 8.8 and 25 °C. *J. Cryst. Growth* 50 (2), 470–480.
- Riechelmann, S., Schröder-Ritzrau, A., Wassenburg, J.A., Schreuer, J., Richter, D.K., Riechelmann, D.F.C., Terente, M., Constantin, S., Mangini, A., Immenhauser, A., 2014. Physicochemical characteristics of drip waters: influence on mineralogy and crystal morphology of recent cave carbonate precipitates. *Geochim. Cosmochim. Acta* 145, 13–29.
- Rodríguez-Navarro, C., Benning, L.G., 2013. Control of crystal nucleation and growth by additives. *Elements* 9 (3), 203–209.
- Rossi, C., Lozano, R.P., 2016. Hydrochemical controls on aragonite versus calcite precipitation in cave dripwaters. *Geochim. Cosmochim. Acta* 192, 70–96.
- Schmid, S.M., Fügenschuh, B., Kissling, E., Schuster, R., 2004. Tectonic map and overall architecture of the Alpine orogen. *Ecol. Geol. Helv.* 97, 93–117.
- Schönlaub, H.-P., 1982. Die Grauwackenzone in den Eisenerzer Alpen (Österreich). *Jahrb. Geol. B.-A.* 124, 361–423.
- Schulz, O., Vavtar, F., Dieber, K., 1997. Die Siderit- Erzlagerstätte Steirischer Erzberg: Eine geowissenschaftliche Studie, mit wirtschaftlicher und geschichtlicher Betrachtung. *Arch. Lagerst. Forsch. Geol. B.-A.* 20, 65–178.
- Stanley, S.M., 2006. Influence of seawater chemistry on biomineralization throughout phanerozoic time: Paleontological and experimental evidence. *Palaeogeogr. Palaeoclimatol. Palaeoecol.* 232, 214–236.
- Sun, W., Jayaraman, S., Chen, W., Persson, K.A., Ceder, G., 2015. Nucleation of metastable aragonite CaCO_3 in seawater. *Proc. Natl. Acad. Sci.* 112 (11), 3199–3204.
- Swart, P.K., 2015. The geochemistry of carbonate diagenesis: the past, present and future. *Sedimentology* 62, 1233–1304.
- Thalmann, F., 1979. Zur Eisenspatvererzung in der nördlichen Grauwackenzone am Beispiel des Erzberges bei Eisenerz und Radmer/Bucheck. *Verh. Geol. B.-A.* 3, 479–489.
- Wassenburg, J., Immenhauser, A., Richter, D.K., Jochum, K.P., Fietzke, J., Deininger, M., Goos, M., Scholz, D., Sabaoui, A., 2012. Climate and cave control on Pleistocene/Holocene calcite-to-aragonite transitions in speleothems from Morocco: Elemental and isotopic evidence. *Geochim. Cosmochim. Acta* 92, 23–47.
- Wassenburg, J.A., Scholz, D., Jochum, K.P., Cheng, H., Oster, J., Immenhauser, A., Richter, D.K., Häger, T., Jamieson, R.A., Baldini, J.U.L., Hoffmann, D., Breitenbach, S.F.M., 2016. Determination of aragonite trace element distribution coefficients from speleothem calcite–aragonite transitions. *Geochim. Cosmochim. Acta* 190, 347–367.